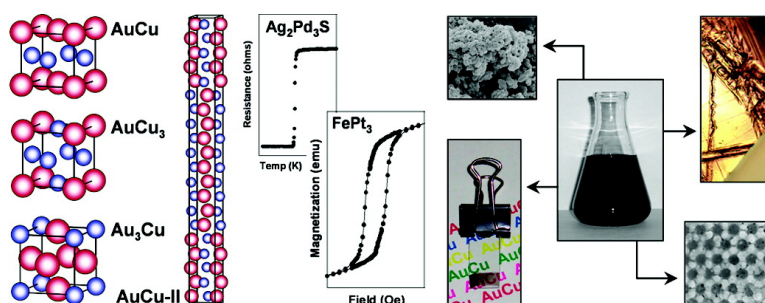# J|A|C|S
JOURNAL OF THE AMERICAN CHEMICAL SOCIETY

Article

Metallurgy in a Beaker: Nanoparticle Toolkit for the Rapid Low-Temperature Solution Synthesis of Functional Multimetallic Solid-State Materials

Raymond E. Schaak, Amandeep K. Sra, Brian M. Leonard, Robert E. Cable, John C. Bauer, Yi-Fan Han, Joel Means, Winfried Teizer, Yolanda Vasquez, and Edward S. Funck

More About This Article

Additional resources and features associated with this article are available within the HTML version:

- Supporting Information
- Links to the 16 articles that cite this article, as of the time of this article download
- Access to high resolution figures
- Links to articles and content related to this article
- Copyright permission to reproduce figures and/or text from this article

View the Full Text HTML

Metallurgy in a Beaker: Nanoparticle Toolkit for the Rapid Low-Temperature Solution Synthesis of Functional Multimetallic Solid-State Materials

Raymond E. Schaak,*,[†] Amandeep K. Sra,[†] Brian M. Leonard,[†] Robert E. Cable,[†] John C. Bauer,[†] Yi-Fan Han,[‡] Joel Means,[‡] Winfried Teizer,[‡] Yolanda Vasquez,[†] and Edward S. Funck[†]

Contribution from the Departments of Chemistry and of Physics, Texas A&M University, College Station, Texas 77842-3012

Received November 4, 2004; E-mail: schaak@mail.chem.tamu.edu

Abstract: Intermetallic compounds and alloys are traditionally synthesized by heating mixtures of metal powders to high temperatures for long periods of time. A low-temperature solution-based alternative has been developed, and this strategy exploits the enhanced reactivity of nanoparticles and the nanometer diffusion distances afforded by binary nanocomposite precursors. Prereduced metal nanoparticles are combined in known ratios, and they form nanomodulated composites that rapidly transform into intermetallics and alloys upon heating at low temperatures. The approach is general in terms of accessible compositions, structures, and morphologies. Multiple compounds in the same binary system can be readily accessed; e.g., AuCu, $AuCu_3$, Au_3Cu, and the AuCu–II superlattice are all accessible in the Au–Cu system. This concept can be extended to other binary systems, including the intermetallics $FePt_3$, CoPt, CuPt, and Cu_3-Pt and the alloys Ag–Pt, Au–Pd, and Ni–Pt. The ternary intermetallic Ag_2Pd_3S can also be rapidly synthesized at low temperatures from a nanocomposite precursor comprised of Ag_2S and Pd nanoparticles. Using this low-temperature solution-based approach, a variety of morphologically diverse nanomaterials are accessible: surface-confined thin films (planar and nonplanar supports), free-standing monoliths, nanomesh materials, inverse opals, and dense gram-scale nanocrystalline powders of intermetallic AuCu. Importantly, the multimetallic materials synthesized using this approach are functional, yielding a room-temperature Fe–Pt ferromagnet, a superconducting sample of Ag_2Pd_3S ($T_c = 1.10$ K), and a $AuPd_4$ alloy that selectively catalyzes the formation of H_2O_2 from H_2 and O_2. Such flexibility in the synthesis and processing of functional intermetallic and alloy materials is unprecedented.

Introduction

Intermetallic compounds and alloys are among the most important solid-state materials in modern science and technology.[1] They possess a surprisingly diverse range of physical properties, including ferromagnetism,[2,3] superconductivity,[4] shape-memory effects,[5] catalytic activity,[6–8] hydrogen storage,[9] structural hardness,[10] and corrosion resistance,[11] and thus find widespread use in many applications.[12] As for all solid-state materials, the synthesis of these multimetallic compounds is crucial for controlling their performance in advanced applications. The possibility of integrating the well-established properties of intermetallic compounds with emerging nanotechnological applications has generated a renewed interest in controlling their synthesis. Controlling the nanostructure and morphology of multimetallic materials is particularly important, as these are the critical factors that limit their utility in future applications.

[†] Department of Chemistry.

[‡] Department of Physics.

(1) Cahn, R. W. *Contemp. Phys.* **2001**, *42*, 365–375.

(2) Sun, S.; Murray, C. B.; Weller, D.; Folks, L.; Moser, A. *Science* **2000**, *287*, 1989–1992.

(3) (a) Goll, D.; Kronmuller, H. *Naturwissenschaften* **2000**, *87*, 423–438. (b) Paduani, C. *J. Appl. Phys.* **2001**, *90*, 6251.

(4) For example, (a) Gavaler, J. R.; Janocko, M. A.; Bradinski, A. I.; Rowland, G. W. *IEEE Trans. Magn.* **1975**, *2*, 192–196. (b) Cava, R. J.; Takagi, H.; Zandbergen, H. W.; Krajewski, J. j.; Peck, W. F.; Siegrist, T.; Batlogg, B.; Vandover, R. B.; Felder, R. J.; Mizuhashi, K.; Lee, J. O.; Eisaki, H.; Uchida, S. *Nature* **1994**, *367*, 252. (c) Cava, R. J.; Takagi, H.; Batlogg, B.; Zandbergen, H. W.; Krajewski, J. J.; Peck, W. F.; Vandover, R. B.; Felder, R. J.; Siegrist, T.; Mizuhashi, K.; Lee, J. O.; Eisaki, H.; Carter, S. A.; Uchida, S. *Nature* **1994**, *367*, 146. (d) Nagamatsu, J.; Makagawa, N.; Muranaka, T.; Zenitani, Y.; Akimitsu, J. *Nature* **2001**, *410*, 63–64. (e) He, T.; Huang, Q.; Ramirez, A. P.; Wang, Y.; Regan, K. A.; Rogado, N.; Hayward, M. A.; Haas, M. K.; Slusky, J. S.; Inumara, K.; Zandbergen, H. W.; Ong, N. P.; Cava, R. J. *Nature* **2001**, *411*, 54–56.

(5) Stern, R. A.; Willoughby, S. D.; MacLaren, J. M.; Cui, J.; Pan, Q.; James, R. D. *J. Appl. Phys.* **2003**, *93*, 8644–8646.

(6) Roucoux, A.; Schulz, J.; Patin, H. *Chem. Rev.* **2002**, *102*, 3757–3778.

(7) (a) Casado-Rivera, E.; Gal, Z.; Angelo, A. C. D.; Lind, C.; DiSalvo, F. J.; Abruna, H. D. *ChemPhysChem* **2003**, *4*, 193–199. (b) Casado-Rivera, E.; Volpe, D. J.; Alden, L.; Lind, C.; Downie, C.; Vazquez-Alvarez, T.; Angelo, A. C. D.; DiSalvo, F. J.; Abruna, H. D. *J. Am. Chem. Soc.* **2004**, *126*, 4043–4049.

(8) Zhang, C. J.; Baxter, R. J.; Hu, P.; Alavi, A.; Lee, M.-H. *J. Chem. Phys.* **2001**, *115*, 5272–5277. Mathauser, A. T.; Teplyakov, A. V. *Catal. Lett.* **2001**, *73*, 207–210.

(9) (a) Kirchheim, R.; Mutschele, T.; Keininger, W.; Gleiter, H.; Birringer, R.; Koble, T. D. *Mater. Sci. Eng.* **1988**, *99*, 457–462. (b) Kamakoti, P.; Sholl, D. S. *J. Membr. Sci.* **2003**, *225*, 145–154.

(10) Liu, C. T. *Mater. Chem. Phys.* **1995**, *42*, 77–86.

(11) Lopez, M. F.; Escudero, M. L. *Electrochim. Acta* **1998**, *43*, 671–678.

(12) (a) Liu, C. T.; Stringer, J.; Mundy, J. N.; Horton, L. L.; Angelini, P. *Intermetallics* **1997**, *5*, 579–596. (b) Stoloff, N. S.; Liu, C. T.; Deevi, S. C. *Intermetallics* **2000**, *8*, 1313–1320.

Intermetallics and alloys are typically synthesized using traditional metallurgical techniques, which include powder reactions and arc melting. Both of these strategies require high-temperature heating (usually >1000 °C) and annealing for long periods of time (often days or weeks). While a few alternative approaches exist for controlling the nanostructure and morphology of multimetallic materials,[13−16] low-temperature solution-based synthetic strategies do not exist. This is in contrast to many other classes of materials, where well-established solution routes are ubiquitous, e.g., sol−gel synthesis of oxides[17] and spin coating of polymer and chalcogenide films.[18]

We recently discovered that, under appropriate conditions, binary mixtures of weakly stabilized Au and Cu nanoparticles aggregate to form binary nanocomposites, which can thermally transform into intermetallic nanocrystals at low temperatures.[19] Our subsequent work showed that this approach can be significantly expanded to include other bimetallic and trimetallic systems with a variety of compositions and accessible crystal structures. Furthermore, the synthetic process can be modified and scaled up to yield bulk and thin-film materials with controlled nanostructure and morphology. Accordingly, we describe here a generalized solution-based synthetic approach—"metallurgy in a beaker"—that uses metal nanoparticles as a robust toolkit for synthesizing morphologically diverse intermetallics and alloys. By using preformed nanoparticles of known metal ratios, multimetallic compounds of those ratios can be made by exploiting the nanoscale intermixing of the nanoparticles. This approach effectively separates the diffusion and nucleation steps, and eliminates solid−solid diffusion as the rate-limiting step in bulk-scale solid-state synthesis. Furthermore, the materials made by this method are functional, yielding properties that match or are superior to similar materials made by traditional routes. In this work, we establish the viability of this new synthetic paradigm for producing functional multimetallic solid-state materials with unprecedented synthetic flexibility.

Experimental Section

Synthesis of Binary and Ternary Intermetallics and Alloys. Au−Cu nanocomposites were synthesized in a manner similar to that of our previous report.[19] Briefly, $Cu(C_2H_3O_2)_2 \cdot H_2O$ (6.8 mg, 0.034 mmol; Alfa Aesar, 98.0−102.0%), $HAuCl_4 \cdot 3H_2O$ (13.3 mg, 0.036 mmol; Alfa Aesar, 99.99%), and poly(vinylpyrrolidone) (PVP; MW = 40000, 120 mg) were added to 25 mL of distilled, deionized water (NANOpure, 18.2 MΩ). (Note that water was the only solvent used in the synthesis of these materials.) After the mixture was stirred for at least 30 min under Ar, 25 mL of 0.01 M $NaBH_4$ (Alfa Aesar, 98%) was added to form a mixture of Au and Cu nanoparticles. After 3−6 h, the resulting nanocomposite was isolated in powder form by centrifugation (including

several washing steps), and dried under ambient conditions. The powder was then annealed at 300 °C under flowing Ar. $AuCu_3$ was synthesized in the same way, using 10.1 mg (0.0505 mmol) and 6.1 mg (0.0168 mmol) of $Cu(C_2H_3O_2)_2 \cdot H_2O$ and $HAuCl_4 \cdot 3H_2O$, respectively. In some cases, poly(styrenesulfonic acid) sodium salt (PSS) (Alfa Aesar, MW = 70000) and poly(2-ethyl-2-oxazoline) (PEO) (Alfa Aesar, MW = 50000) were used instead of PVP. Other binary phases (Ag−Pt, Au−Pd, Co−Pt, Cu−Pt, Fe−Pt, Ni−Pt) were synthesized using similar molar ratios and the following metal salt precursors (obtained from Alfa Aesar): $AgNO_3$ (99.9+%), K_2PtCl_6 (40.11% Pt), $PdCl_2$ (99.9%), $CoCl_2 \cdot 6H_2O$ (98.0−102.0%), $FeCl_2 \cdot xH_2O$ (99%), and $Ni(C_2H_3O_2) \cdot xH_2O$ (99+%). The ternary phase Ag_2Pd_3S was synthesized as follows: PVP-stabilized Ag_2S nanoparticles were synthesized according to ref 20 using $AgNO_3$ and $Na_2S \cdot 9H_2O$ (Alfa Aesar, 98.0−103.0%), washed, dried, and then added to a fresh aqueous solution of PVP-stabilized Pd nanoparticles synthesized according to ref 21. The final concentrations of Ag_2S and Pd used to form the nanocomposite were 18 and 1 mg/mL, respectively. The resulting nanocomposite was isolated by centrifugation and annealed at 300 °C under Ar.

Synthesis of Morphologically Diverse Nanomaterials. Thin films were prepared by solution evaporation. A glass slide precleaned in piranha solution (3:1 H_2SO_4/H_2O_2) was placed upright in a beaker containing the Au−Cu nanocomposite solution (recovered, washed, and redispersed to an approximate concentration of 5 mg/mL), which was allowed to evaporate in a fume hood. The resulting black Au−Cu nanocomposite film was converted to a film of intermetallic AuCu by annealing for 30 min at 300 °C in flowing Ar. To prepare free-standing films, the Au−Cu nanocomposite synthesis was scaled up by a factor of 20, and centrifuged in a round-bottom centrifuge tube to slowly precipitate the nanocomposite. Upon washing and drying, a free-standing nanocomposite was formed, and its surface features conformed to the surface of the centrifuge tube (showing microscale scratches). The free-standing Au−Cu nanocomposite was converted to intermetallic AuCu by annealing for 30 min at 300 °C in flowing Ar.

Nanostructured materials were synthesized by replicating against sacrificial templates. An inverse opal (colloidal crystal replica) was synthesized by infiltrating a colloidal crystal comprised of 1.0 µm polystyrene beads (prepared by centrifuging an aqueous suspension of polymer beads as obtained from Interfacial Dynamics Corp.) with the Au−Cu nanocomposite, drying under ambient conditions, and then annealing to 350 °C under flowing Ar to remove the polystyrene beads and to crystallize the framework. A disordered porous nanomesh material was synthesized in a similar manner, using a disordered aggregate of polystyrene beads instead of a periodic colloidal crystal.

Characterization and Physical Property Measurements. Powder X-ray diffraction (XRD) data were collected on a Bruker GADDS three-circle X-ray diffractometer using Cu Kα radiation. Differential scanning calorimetry (DSC) data were collected on a TA Instruments Q600 SDT under an Ar purge. Elemental analysis (CHN) was performed by Atlantic Microlab (Norcross, GA). Inductively coupled plasma (ICP) elemental analysis results were obtained using a Perkin-Elmer DRCII ICP-MS. X-ray photoelectron spectroscopy (XPS) measurements were acquired on a Kratos Ultra Axis Hsi 165 XPS using an Al anode set at 15 mA and 15 kV. Samples were prepared by sonicating the nanoparticles in ethanol, dropping a dilute suspension on a clean Si wafer, and then drying. Transmission electron microscopy (TEM) images, selected area electron diffraction (SAED) patterns, and energy-dispersive X-ray analysis (EDS) were acquired using a JEOL JEM-2010 transmission electron microscope. Scanning electron microscopy (SEM) images were obtained at 15 kV using a JEOL JSM-6400 SEM. Optical microscope images were acquired on a Zeiss AxioSkop 2-MAT operating in reflection mode. Magnetic susceptibility and magnetization measure-

(13) (a) Gleiter, H. *Prog. Mater. Sci.* **1989**, *33*, 223−315. (b) Suryanarayana, C. *Prog. Mater. Sci.* **2001**, *46*, 1−184.
(14) (a) Hahn, H. *Nanostruct. Mater.* **1997**, *9*, 3−12. (b) Koch, C. C. *Nanostruct. Mater.* **1997**, *9*, 13−22.
(15) Blair, R. G.; Gillan, E. G.; Nguyen, N. K. B.; Daurio, D.; Kaner, R. B. *Chem. Mater.* **2003**, *15*, 3286−3293.
(16) (a) Novet, T.; Johnson, D. C. *J. Am. Chem. Soc.* **1991**, *113*, 3398−3403. (b) Noh, M.; Thiel, J.; Johnson, D. C. *Science* **1995**, *270*, 1181−1184. (c) Noh, M.; Johnson, C. D.; Hornbostel, M. D.; Thiel, J.; Johnson, D. C. *Chem. Mater.* **1996**, *8*, 1625−1635.
(17) Wright, J. D.; Sommerdijk, A. J. M. *Sol-gel materials: chemistry and applications*; Gordon and Breach: Amsterdam, 2001.
(18) (a) Madou, M. J. *Fundamentals of Microfabrication: The Science of Miniaturization*, 2nd ed.; CRC Press: Boca Raton, FL, 2002. (b) Mitzi, D. B.; Kosbar, L. L.; Murray, C. E.; Copel, M.; Afzali, A. *Nature* **2004**, *428*, 299−303.
(19) Sra, A. K.; Schaak, R. E. *J. Am. Chem. Soc.* **2004**, *126*, 6667−6672.

(20) Gao, F.; Lu, Q.; Zhao, D. *Nano Lett.* **2003**, *3*, 85−88.
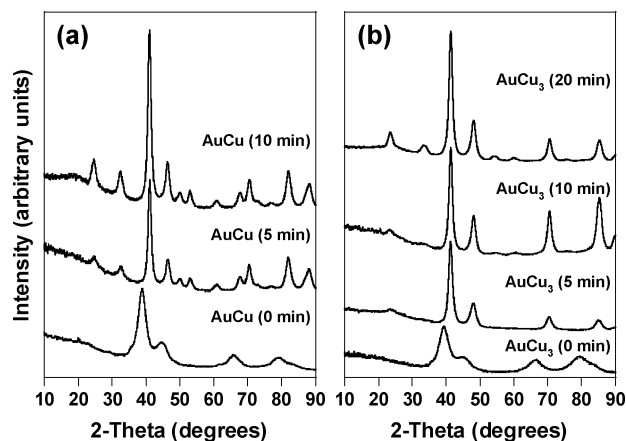(21) Lu, W.; Wang, B.; Wang, K.; Wang, X.; Hou, J. G. *Langmuir* **2003**, *9*, 5887−5891.

Figure 1. Powder XRD patterns showing the time-resolved transformation of (a) AuCu and (b) AuCu₃ nanocomposites into intermetallic AuCu and AuCu₃, respectively, at 300 °C. The samples labeled "0 min" correspond to the room-temperature nanocomposite (not heated), and the listed heating times refer to the length of time the sample remained in the furnace after the furnace reached 300 °C.

ments were carried out on a Quantum Design SQUID magnetometer MPMS-XL. Magnetization vs applied field data were collected in the $0-6.5$ T range at 10 K. Low-temperature resistivity data characterizing the superconducting transition of Ag_2Pd_3S were acquired on a home-built dilution refrigerator, using a standard four-wire ac lock-in (PAR 124A) technique ($f = 23$ Hz) with an RMS excitation current of 0.5 mA. The temperature was measured using a factory-calibrated Ge resistor (Lake Shore Cryotronics GR-200A-100).

Catalytic reactions were carried out at atmospheric pressure and at 10 °C in the reactor described in ref 22. The experiment was carried out using a 4:1 O_2/H_2 gas mixture at a total flow rate of 50 mL/min in a 0.24 N H_2SO_4/ethanol solution. *Since the 4:1 O_2/H_2 gas mixture is in the explosive regime, care was taken to avoid contact of the gas mixture with a dry catalyst*. This was achieved by first mixing 5 mg of the catalyst with 10 mL of the solution and returning this slurry to the solution that remained in the reactor. Even with this precaution, *explosions did occur* with ethanol as the liquid phase. The use of methanol was even more hazardous because of its higher vapor pressure. The reagent gases were introduced into the reactors via a fine glass frit, and the slurry containing the catalyst was stirred to minimize diffusion limitations. The reactor was connected to a gas chromatograph so that the concentration of H_2 exiting the reactor could be periodically determined. Improved accuracy in the H_2 analysis was achieved by using a H_2/N_2 mixture that contained 10% N_2. The H_2O_2 formed during the reaction was analyzed colorimetrically after complexation with a $TiOSO_4/H_2SO_4$ reagent. The selectivity for H_2O_2, $S_{H_2O_2}$, was determined from the rate of H_2O_2 formation and the rate of H_2 conversion using the equation

$$S_{H_2O_2} = \frac{\text{rate of H}_2\text{O}_2 \text{ formation (mol/min)}}{\text{rate of H}_2 \text{ conversion (mol/min)}} \times 100 \qquad (1)$$

Results and Discussion

Au−Cu System: Synthesis and Characterization. Stoichiometric molar ratios of Au and Cu metal salt precursors were reduced in solution by $NaBH_4$ in the presence of PVP to form nanoparticle mixtures, which were aged to form binary Au−Cu nanocomposite precipitates with compositions that were closely related to the initial ratios of Au and Cu that were present prior to reduction. The resulting powders were annealed under Ar to study their thermal transformation. Figure 1 shows time-

(22) Chinta, S.; Lunsford, J. H. *J. Catal.* **2004**, *225*, 249.

resolved XRD data for AuCu and AuCu₃ nanocomposites heated to 300 °C. Prior to heating, only Au is crystalline, and the XRD pattern matches that expected for Au. This is consistent with earlier results.[19] However, after only 5 min of heating at 300 °C, the ordered intermetallic compound AuCu is formed, and further heating increases its crystallinity. Similar results are obtained for AuCu₃, although the ordered phase only begins to appear after 10 min, and is fully formed within 20 min. Interestingly, complete interdiffusion of Cu and Au occurs within 5 min to form a disordered AuCu₃ alloy, while slightly longer heating is required to nucleate the ordered intermetallic polymorph. The diffusion and nucleation events have been separated using the nanocomposite precursors, which contain domains of Au and Cu that are modulated at the nanoscale. This is a rough 3D analogy to work by Johnson and co-workers on elementally modulated thin films, which show similar reactivity.[16] The nanometer diffusion distances support low-temperature diffusion without the high-temperature melting step that is necessary in traditional metallurgy. Likewise, the PVP confines the crystallites to nanoscale dimensions, allowing atomic ordering to occur rapidly without long-term annealing.

Time-resolved XRD data for the traditional powder metallurgical synthesis of AuCu provides a dramatic comparison of the reaction kinetics at 300 °C (Supporting Information). Even after 2 h of heating, only Au and Cu are detectable. The absence of peaks from AuCu suggests that any AuCu that may be present exists either in small quantities (<5% of the sample) or in nanoscale interfacial domains. After 24 h of heating at 300 °C, Au and Cu still dominate the XRD pattern, although the 111 peak of AuCu is detectable as a low-intensity broad reflection around 41° (detected by careful comparison to the baseline). Clearly, the nanoscale intermixing of prereduced metal particles (a) significantly increases the reaction kinetics relative to traditional syntheses involving micrometer-sized powders and (b) eliminates the need for high-temperature arc-melting, which is usually necessary to facilitate homogeneous interdiffusion in these systems.

EDS analyses of multiple regions of the samples confirm that Au and Cu are present in approximately 1:1 and 1:3 molar ratios for AuCu and AuCu₃, respectively. TGA analysis indicates that most of the polymer coating is removed by 450 °C, and shows that 13.7% (by mass) of the nanocomposite precursor consists of PVP. However, CHN analysis of the product heated to 500 °C shows some residual carbon (approximately 2.0%). The reaction yields are typically between 85% and 95%, based on the theoretical yield expected from the amounts of Au and Cu used in the reaction and the amount of polymer present in the nanocomposite precursor.

In addition to PVP, other polymer stabilizers can be used in the nanocomposite-based synthesis of alloys and intermetallics. For example, intermetallic AuCu forms when PSS or PEO is used instead of PVP (Supporting Information). The yields for these polymers are lower than for PVP (30−40%), but the nucleation and order/disorder transition temperatures are similar. Importantly, TGA analysis indicates that most of the PEO is burned off by 275 °C, and only 0.2% residual carbon is detected by CHN analysis of the product heated to 500 °C. For PSS, most of the polymer is removed by heating to 400 °C, and CHN analysis indicates 0.6% residual carbon. Thus, the possibility
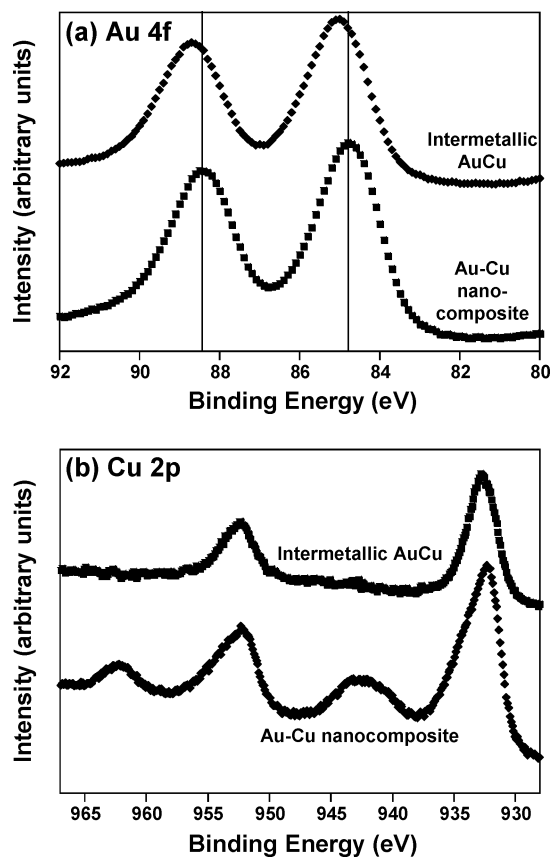
Figure 2. XPS core level spectra for the (a) Au 4f and (b) Cu 2p regions of a 1:1 Au−Cu nanocomposite and the corresponding nanocrystalline intermetallic phase formed after heating of the nanocomposite to 300 °C for 30 min. The lines in (a) highlight the Au 4f peak shifts, which indicate the formation of an alloy phase.

exists for controlling the carbon content by carefully choosing the polymer stabilizer and its decomposition properties.

XPS spectra for the AuCu and $AuCu_3$ samples show no evidence for impurities related to the chemical precursors. Specifically, no B, Na, or Cl was detected, and this was confirmed with ICP data. It is well-known that nanoparticle formation using borohydride reduction of metal salts can lead to metal boride impurities.[23] However, prior studies of Au and Cu nanoparticles prepared by this route show no boron incorporation,[24] and our findings are consistent with this. Figure 2 shows XPS spectra for the Au 4f and Cu 2p core level regions of the AuCu nanocomposite precursor and the intermetallic AuCu product. The Au:Cu ratio, based on multiple XPS analyses, is 1.0:1.1 (e.g., $AuCu_{1.1}$), which is consistent with the EDS data. The spectra show features that are expected for zerovalent Au and Cu, along with some oxidized Cu. The Au 4f region of the AuCu nanocomposite precursor shows peaks matching those for metallic Au. Relative to those for pure Au metal, the peaks for the intermetallic AuCu product are shifted to higher binding energies by approximately 0.25 eV. Similar shifts have been observed previously for Au−Cu alloy nano-
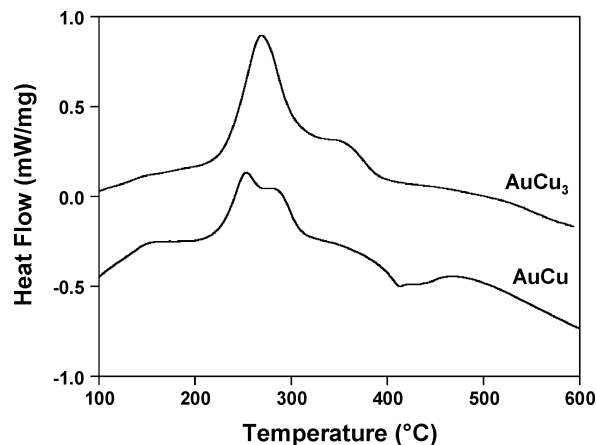

Figure 3. DSC trace for binary Au−Cu nanocomposites with 1:1 and 1:3 stoichiometries, showing the formation of AuCu and $AuCu_3$, respectively. Positive output is exothermic.

particles, and they indicate the formation of a compound with atomic-scale mixing of Au and Cu.[25]

The Cu 2p region of the nanocomposite precursor is complex, showing several overlapping peaks that match those expected for a mixture of metallic Cu and oxidized Cu. Deconvolution of the peaks (Supporting Information) yields a relative population of 68.8% Cu^0, 4.0% Cu^{1+}, and 27.2% Cu^{2+}. The Cu 2p region of the XPS spectrum for the intermetallic AuCu sample shows primarily metallic Cu. Analysis of $AuCu_3$ samples showed similar results. The presence of a large amount of Cu^{2+} in the room-temperature nanocomposite sample is not unexpected, since postsynthesis sample handling was not performed in an air-free environment. The weakly stabilized copper nanoparticles that comprise the nanocomposite precursor are known to oxidize quickly under ambient conditions.

AuCu and $AuCu_3$ are model systems for order−disorder phase transitions in bulk materials, and the thermodynamics of their formation has been studied extensively for samples of homogenized Au−Cu alloys prepared by arc-melting and annealing.[26−29] DSC data for our AuCu and $AuCu_3$ nanocomposite samples, with inherent nanoscale intermixing of Au and Cu resulting from the spontaneous room-temperature aggregation of prereduced metal nanoparticles, are shown in Figure 3. Our data appear similar to the data reported previously for bulk samples. The broad exotherms below 200 °C are attributed to interdiffusion of the Au and Cu. For the AuCu sample, exotherms centered near 250 and 280 °C have been observed previously and correspond to ordering of the AuCu solid solution into the intermetallic structure.[27] The broad endotherm centered near 415 °C results from the disordering of the intermetallic AuCu, as well as decomposition of the PVP at slightly higher temperatures. A previous calorimetric study of nanocrystalline AuCu films suggested that ordering and disordering transitions begin at grain boundaries due to enhanced mobility and the presence of vacancies, and that impurities do not influence the calorimetric data.[28] Our results are consistent with these observations.

(23) (a) Schlesinger, H. I.; Brown, H. C.; Finholt, A. E.; Gilbreath, J. R.; Hoekstra, H. R.; Hyde, E. K. *J. Am. Chem. Soc.* **1953**, *75*, 215−219. (b) Corrias, A.; Ennas, G.; Licheri, G.; Marongiu, G.; Paschina, G. *Chem. Mater.* **1990**, *2*, 363−366.

(24) (a) Bonnemann, H.; Brijoux, W.; Brinkmann, R.; Fretzen, R.; Joussen, T.; Koppler, R.; Korall, B.; Neiteler, P.; Richter, J. *J. Mol. Catal.* **1994**, *86*, 129−177. (b) Glavee, G. N.; Klabunde, K. J.; Sorensen, C. M.; Hadji-panayis, G. C. *Langmuir* **1994**, *10*, 4726−4730.

(25) (a) Sangregorio, C.; Galeotti, M.; Bardi, U.; Baglioni, P. *Langmuir* **1996**, *12*, 5800−5802. (b) Kim, M.-J.; Na, H.-J.; Lee, K. C.; Yoo, E. A.; Lee, M. *J. Mater. Chem.* **2003**, *13*, 1789−1792.

(26) (a) Tissot, P.; Dallenbach, R. *Thermochim. Acta* **1978**, *25*, 143−153. (b) Feutelais, Y.; Legendre, B.; Guymont, M. *Acta Mater.* **1999**, *47*, 2539−2551.

(27) Battezzati, L.; Belotti, M.; Brunella, V. *Scr. Mater.* **2001**, *44*, 2759−2764.

(28) Battezzati, L.; Barbero, S.; Belotti, M.; Riontino, G. *Z. Metallkd.* **2003**, *94*, 449−452.

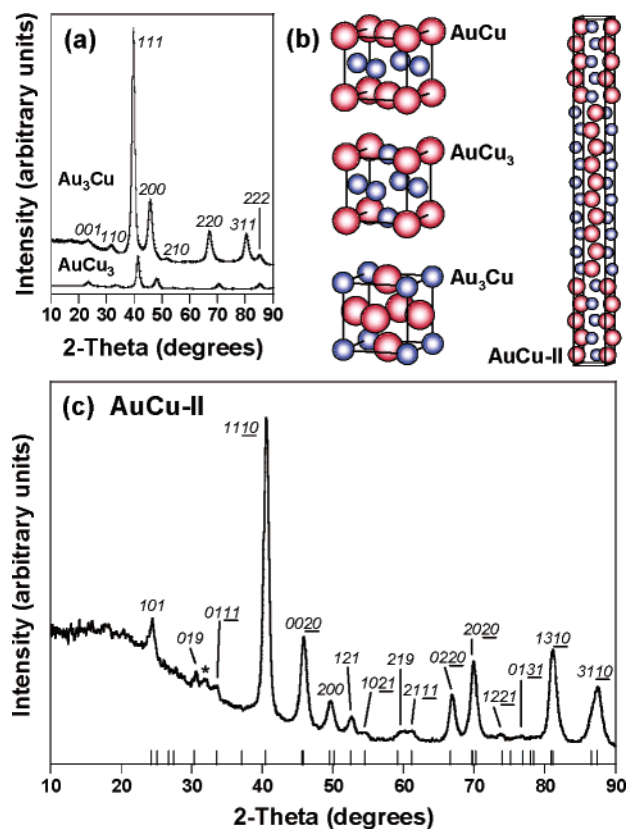(29) Sprusil, B.; Xima, V.; Chalupa, B.; Smola, B. *Z. Metallkd.* **1993**, *84*, 2.

Figure 4. (a) Powder XRD patterns for Au$_3$Cu (synthesized at 240 °C) and Cu$_3$Au (for comparison, since Cu$_3$Au has a significantly smaller unit cell than Au$_3$Cu), (b) structures of the four Au−Cu compounds accessed using nanocomposite precursors (based on crystallographic information in ref 31), and (c) powder XRD pattern for the AuCu-II superlattice formed by heating a PEO-stabilized Au−Cu nanocomposite to 360 °C. The asterisk in (c) represents an intermetallic AuCu impurity. The remaining peaks for the AuCu impurity overlap the fundamental peaks of the AuCu-II superlattice. The tick marks in (c) indicate the allowed reflections for the AuCu-II superlattice.

DSC data for the AuCu$_3$ sample are similar (Figure 3), although only one exotherm corresponding to the formation of ordered AuCu$_3$ is observed. Again, this is consistent with literature reports.[29] The disorder temperature is lower than for AuCu, and this is also consistent with previous calorimetry data,[29] as well as the equilibrium phase diagram.

XRD data confirm the assignments of the thermodynamic transitions discussed above, including diffusion, nucleation of the ordered phases, and the order−disorder transition. However, using PVP as a surface stabilizer, we could not isolate the AuCu-II superlattice, which is known to form in the Au−Cu system just before disordering occurs.[30−32] We could, however, access AuCu-II using PEO. The AuCu-II superlattice is a long-period antiphase structure, which is shown in Figure 4b. Since it is orthorhombic and the lattice parameter for the c axis is approximately 10 times larger than that of tetragonal (L1$_0$) AuCu, it can be clearly distinguished in the XRD pattern shown in Figure 4c. Specifically, the peaks near 30.5°, 33.5°, and 54.5° are unique to the large AuCu-II superlattice. In addition to

(30) Okamura, K.; Iwasaki, H.; Ogawa, S. *J. Phys. Soc. Jpn.* **1968**, *24*, 569−579.
(31) Villars, P., Calvert, L. D., Eds. *Pearson's Handbook of Crystallographic Data for Intermetallic Phases*, 2nd ed.; ASM International: Materials Park, OH, 1991.
(32) Massalski, T. B., Ed. *Binary Alloy Phase Diagrams*; ASM International: Materials Park, OH, 1996.

Table 1. Summary of Binary Phase Formation

nominal stoichiometry	apparent stoichiometry[a]	crystalline XRD product	alloy temp range,[b] °C	intermetallic temp range,[b] °C
Ag$_3$Pt	Ag$_3$Pt	fcc-type Ag$_3$Pt alloy	100−600	N/A
Au$_2$Cu	Au$_3$Cu	AuCu$_3$-type Au$_3$Cu	100, 300−600	200
AuCu	AuCu	AuCu-type AuCu	100, 500−600	200−400
AuCu$_2$	AuCu$_3$	AuCu$_3$-type AuCu$_3$	100, 500−600	200−400
Au$_3$Pd	Au$_3$Pd	fcc-type Au$_3$Pd alloy	20−600	N/A
AuPd	AuPd$_2$	fcc-type AuPd$_2$ alloy	20−600	N/A
AuPd$_3$	AuPd$_4$	fcc-type AuPd$_4$ alloy	20−600	N/A
CoPt	CoPt	AuCu-type CoPt	20−600	600
Cu$_3$Pt	Cu$_3$Pt	AuCu$_3$-type Cu$_3$Pt	20−300	400−600
CuPt	CuPt	CuPt-type CuPt	20−300	400−600
Fe$_3$Pt	FePt	AuCu-type FePt	20−400	500−600
FePt	FePt$_3$	AuCu$_3$-type FePt$_3$	20−500	600
FePt$_3$	FePt$_3$	AuCu$_3$-type FePt$_3$	20−400	500−600
Ni$_3$Pt	NiPt	fcc-type NiPt alloy	20−600	N/A
NiPt	Ni$_{0.1}$Pt$_{0.9}$	fcc-type Ni$_{0.1}$Pt$_{0.1}$ alloy	20−600	N/A

^{a} Estimated using Vegard's law analysis. ^{b} Temperature range over which alloy and intermetallic phases are observed experimentally.
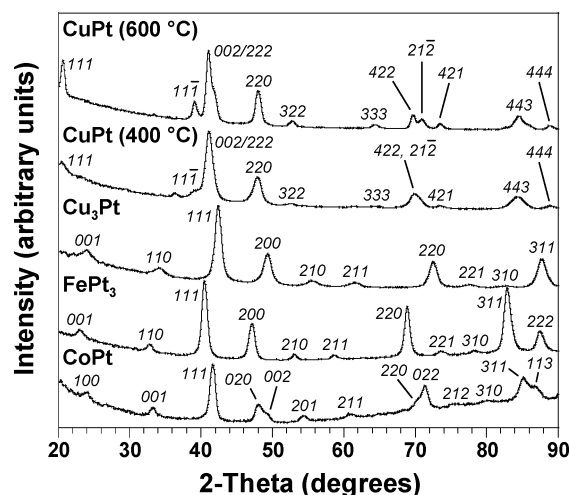

Figure 5. Powder XRD patterns for intermetallic AuCu-type CoPt (600 °C), AuCu$_3$-type FePt$_3$ (500 °C), AuCu$_3$-type Cu$_3$Pt (500 °C), and CuPt-type CuPt (400−600 °C) synthesized from the corresponding binary nanocomposite precursors. Intermetallic CuPt forms by 400 °C, and the peaks that appear in the XRD pattern for the sample heated to 600 °C confirm the rhombohedral structure.

forming the AuCu-II superlattice, Cu$_3$Au-type Au$_3$Cu can be formed by changing the ratios of the metal precursors (Figure 4a). These results for the AuCu system clearly show the versatility of the synthetic process with respect to the range of compositions and structures that are accessible.

Extension to Other Binary Systems. The concept of a nanoparticle toolkit for assembling binary composites that rapidly transform into alloys and intermetallics is general and can be extended to a variety of other binary late-transition-metal systems. The systems studied to date include Ag−Pt, Au−Cu, Au−Pd, Co−Pt, Cu−Pt, Fe−Pt, and Ni−Pt, and these represent a variety of important materials with known magnetic, electronic, optical, and catalytic properties. Table 1 summarizes our results for these systems, highlighting the temperature ranges over which we observe the formation of alloys and intermetallics. XPS and ICP analyses of the products indicate that only the Ni−Pt and Fe−Pt systems have boron impurities (e.g., 2.0% B in Ni$_3$Pt and 0.5% B in FePt$_3$), which is consistent with known boron incorporation in nanoparticles prepared using borohydride reduction.[24] Figure 5 shows XRD data for representative binary phases, which include CoPt (tetragonal, AuCu-type), FePt$_3$ (cubic, AuCu$_3$-type), Cu$_3$Pt (cubic, AuCu$_3$-type), and CuPt (rhombohedral, CuPt-type). All of these crystalline phases were
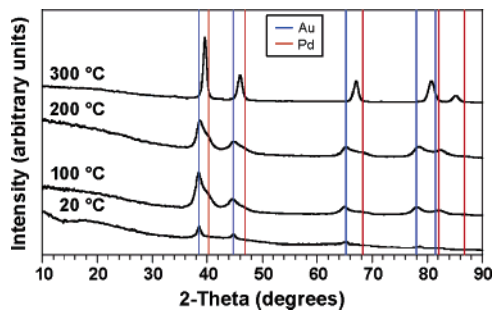
Figure 6. Powder XRD patterns for a Au−Pd nanocomposite heated for 60 min at 20, 100, 200, and 300 °C. Reference lines for Au (blue) and Pd (red) are shown for comparison.

Figure 7. Powder XRD patterns for Pd nanoparticles, Ag_2S nanoparticles, the Ag_2S−Pd nanocomposite (1:3 stoichiometry) at room temperature, and the Ag_2S−Pd nanocomposite heated to 300 and 500 °C for 60 min, showing the formation of intermetallic Ag_2Pd_3S. The tick marks below the peaks for Ag_2Pd_3S (500 °C) represent the peak positions from PDF Card 27-1156 ($AgPd_2S$, which subsequent papers reported to be identical to the Ag_2Pd_3S superconductor). The asterisk in the Ag_2S−Pd room-temperature nanocomposite shows the peaks corresponding to Pd; the remaining peaks match Ag_2S.

formed from nanocomposite precursors that were heated for only 30−60 min. The formation of rhombohedral CuPt is particularly interesting, since its distorted structure has a unique long-range ordering motif that differs from those of the Au−Cu alloys.[33] The rhombohedral superstructure is formed within 30 min of heating at 400 °C, and becomes more crystalline at higher temperatures (Figure 5).

XRD data showing the formation of a Au−Pd alloy (Figure 6) are demonstrative of the low-temperature diffusion afforded by the nanocomposite synthetic route. At 20 °C, Au is crystalline, and Pd is amorphous. At 100 °C, the Pd crystallizes, and both Au and Pd can be seen in the XRD pattern. At 200 °C, Au and Pd are still present as separate phases, although a slight shift (approximately 1−2%) in the lattice constants for Au and Pd suggests that some interdiffusion is starting to occur. By 300 °C, a single phase is present, and the lattice constant is intermediate between those of Au and Pd. On the basis of Vegard's law,[34] the composition of this alloy is closer to $AuPd_2$ than the nominal stoichiometry of AuPd. The difference in composition between the nominal stoichiometry and the actual composition of the product most likely results from incomplete aggregation of the nanoparticle precursors during the solution-phase synthesis of the nanocomposite precursors.

Table 1 indicates differences between the nominal and actual stoichiometries for several of the binary systems studied. These values were derived using Vegard's law,[34] which allows us to estimate the composition of an alloy by comparing its lattice constant with those of the single-metal end members. The fact that we do not observe intermetallics in the Ag−Pt and Ni−Pt systems, where ordered intermetallic compounds are known, is likely because of the difference between the nominal and actual compositions, which places them in a different region of the phase diagram where the intermetallics are not stable.[32]

Extension to a Ternary System. Ternary phases are generally more complex than binary compounds in terms of synthesis, structures, and properties. Forming a nanocomposite of binary and unary nanoparticles allows nanocomposites of ternary compositions to be accessed. These ternary nanocomposites can be thermally processed to form ternary intermetallic phases, in analogy to the binary compounds discussed earlier. This greatly expands the complexity of compositions and structures that are accessible using a nanoparticle toolkit for solid-state synthesis.

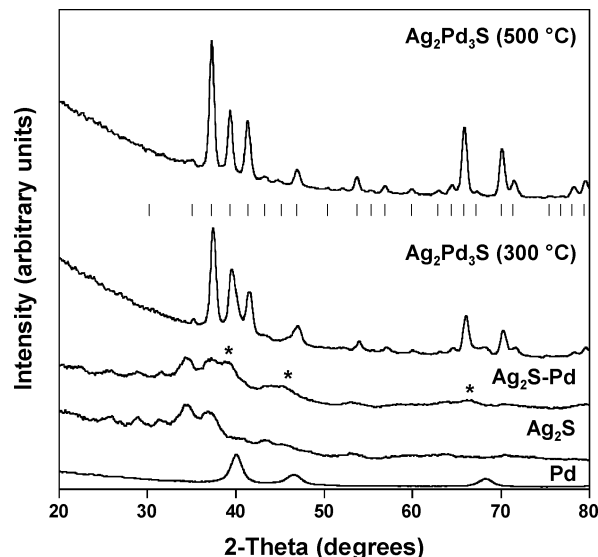For proof-of-concept purposes, we chose the Ag−Pd−S system to demonstrate the formation of a ternary phase.[35−37]

Nanocrystals of Ag_2S and Pd are easily synthesized according to literature methods,[20,21] and can serve as robust precursors to ternary Ag−Pd−S phases. Ag_2S nanocrystals were synthesized,[20] isolated by centrifugation, washed, and then added to a freshly prepared solution of PVP-stabilized Pd nanocrystals[21] in a 1:3 ratio of Ag_2S to Pd. The XRD patterns for powder samples of the Ag_2S and Pd nanoparticles are shown in Figure 7, and the corresponding TEM micrographs and SAED patterns are shown in parts a and b of Figure 8, respectively. Both Ag_2S and Pd nanocrystals are stable in solution, but when they are mixed together, a precipitate begins forming within minutes, and the resulting powder is easily isolated by centrifugation. The Ag_2S and Pd nanoparticles were mixed in a 1:3 ratio, since that stoichiometry (Ag_2Pd_3S) matches a known ternary phase that is superconducting at $T_c = 1.13$ K.[37]

The XRD pattern for this Ag_2S−Pd nanocomposite at room temperature is shown in Figure 7, and the corresponding TEM micrograph is shown in Figure 8c. The XRD pattern has broad peaks that match those expected for Ag_2S and Pd, indicating that both of these phases are present in the nanocomposite. The peaks for Pd are shifted slightly to smaller angles in the Ag_2S−Pd nanocomposite, suggesting that some low-temperature interdiffusion between Ag and Pd is occurring (since the lattice constant for Ag is larger than that for Pd). The TEM micrograph of the Ag_2S−Pd nanocomposite in Figure 8c initially appears to be a large aggregate of many smaller nanoparticles. Upon closer inspection, however, two distinct regions are discernible— a core region that contains a hexagonal superlattice of nearly monodisperse 5 nm nanoparticles, and a surrounding region that

(33) Lang, H.; Mohri, T.; Pfeiler, W. *Intermetallics* **1999**, *7*, 1373−1381.
(34) West, A. R. *Solid State Chemistry and its Applications*; Wiley: Chichester, England, 1984.

(35) (a) Raub, V. E.; Wullhorst, B.; Plate, W. *Z. Metallkd.* **1954**, *45*, 533−537. (b) El-Borady, M.; Schubert, K. *Z. Metallkd.* **1971**, *62*, 667−675.
(36) Villars, P.; Prince, A.; Okamoto, H. *Handbook of Ternary Alloy Phase Diagrams*; ASM International: Materials Park, OH, 1995.
(37) Khan, H. R.; Trunk, H.; Raub, Ch. J.; Fertig, W. A.; Lawson, A. C. *J. Less-Common Met.* **1973**, *30*, 167−168.
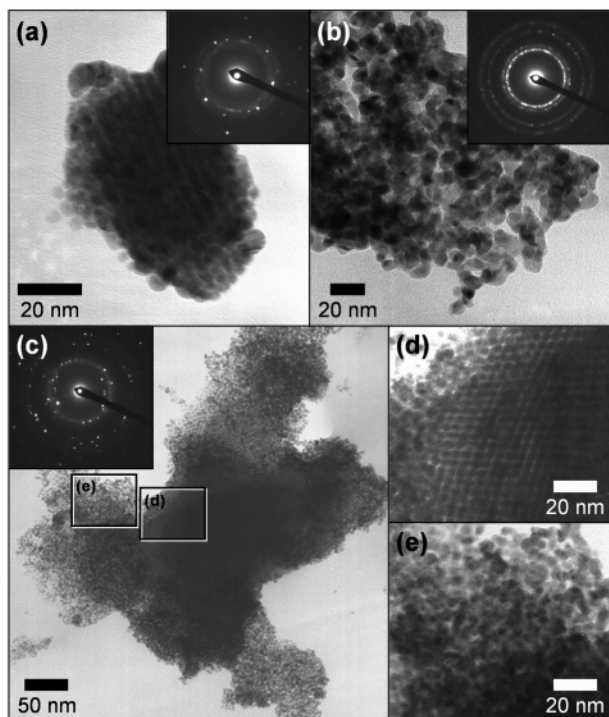
Figure 8. TEM micrographs and SAED patterns for (a) PVP-stabilized Ag_2S nanoparticles, (b) PVP-stabilized Pd nanoparticles, and (c) the Ag_2S–Pd nanocomposite that forms at room temperature from the aggregation of Ag_2S and Pd nanoparticles. Panels d and e are enlarged regions from panel c, showing the Ag_2S and Pd regions of the nanocomposite. EDS spectra are shown as Supporting Information.

contains a random network of irregularly shaped 5–20 nm nanoparticles. Comparison with the TEM micrographs for Ag_2S and Pd nanoparticles in parts a and b of Figure 8, respectively, suggests that the hexagonal superlattice in the Ag_2S–Pd nanocomposite contains Ag_2S nanoparticles, and the surrounding region is made up of Pd nanoparticles. The SAED pattern for the entire aggregate in Figure 8c is complex, and can be indexed to a mixture of Ag_2S and Pd. Likewise, EDS analysis of the entire region in Figure 8c confirms that Ag, Pd, and S are present with an approximate overall composition of $Ag_{2.2}Pd_{2.9}S$ (Supporting Information), and bulk ICP analysis indicates an average composition of $Ag_2Pd_{3.3}S_x$ (the sulfur content was not determined by ICP). These data, combined with the XRD data in Figure 7, confirm that the aggregate in Figure 8c is a composite of Ag_2S and Pd nanoparticles. While this nanocomposite is clearly much larger and less homogeneously mixed than the Au–Cu nanocomposites described earlier, the intermixing of Ag_2S and Pd is still homogeneous at the 50–200 nm scale, and this represents significantly better mixing than is attainable using traditional solid-state synthetic approaches. This nanoscale mixing, combined with the enhanced reactivity of nanoparticles relative to bulk powders, suggests that the Ag_2S–Pd nanocomposite may be easily converted into the ternary Ag_2Pd_3S phase upon rapid low-temperature heating.

DSC data for the Ag_2S–Pd nanocomposite show a broad exotherm starting around 200 °C. Indeed, XRD data confirm that the nanocomposite begins converting to the ternary phase at this temperature. XRD patterns for the Ag_2S–Pd nanocomposite heated for 30 min at 300 and 500 °C are shown in Figure 7. Ag_2Pd_3S adopts the β-Mn structure,[37] which is distinct from any structures that exist in the constituent unary and binary

systems. The XRD data show that the diffusion and nucleation steps are complete within 30 min of heating, yielding the desired ternary phase. This is in contrast to the standard procedure for synthesizing this material, which requires heating at 1000 °C for 2 h, followed by annealing at 550 °C for 3 days.[37] These results establish that (a) the solution-based nanocomposite approach is applicable to ternary phases, (b) nanoparticle composites form between metals and semiconductors, and (c) these metal–semiconductor nanocomposite precursors react similarly to the metal–metal binary composites to form ternary phases.

Morphologically Diverse Nanomaterials. An important consequence of this solution-based synthetic approach is that it can be scaled up to yield morphologically diverse intermetallic and alloy materials. Multimetallic materials with controlled shape, size, and dimensionality can be readily accessed using solution-deposition techniques and nanoscale templating strategies. Such flexibility in materials processing is unprecedented for intermetallics and alloys.

Thin films of intermetallics and alloys can be prepared by common solution-deposition techniques, including evaporation and spin coating. Figure 9a shows an optically transparent film of intermetallic AuCu that was prepared by evaporating an aqueous solution of the binary Au–Cu nanocomposite onto a clean glass slide, and then annealing the film at 300 °C for 30 min. XRD patterns confirm the ordered intermetallic structure of AuCu. SEM micrographs (Figure 9b,c) show a uniform film with an average thickness of 10 μm. The enlarged region in Figure 9c highlights the nanoscale grains that comprise the films, as well as the local surface roughness. Preliminary evidence suggests that this approach to thin film growth can also be extended to polymer supports and spin-coated surfaces. In addition to planar films, this solution-based strategy can be used to synthesize intermetallic and alloy films on nonplanar surfaces. Figure 9d shows a photograph of a glass rod that was coated with a film of intermetallic AuCu by dipping the rod in a Au–Cu nanocomposite solution, allowing the solution to evaporate, and then heating the rod to 300 °C for 30 min.

By scaling up the thin film deposition process, free-standing multimetallic films and membranes can also be formed by drying a nanocomposite solution onto a molded surface. Figure 9e shows a free-standing Au–Cu–PVP nanocomposite. The nanocomposite precursor thermally transforms to an intermetallic AuCu monolith, which is shown in Figure 9f. The change in color from black to metallic golden is indicative of the change in structure and grain growth that occur during thermal processing. Optical micrographs of the intermetallic AuCu monoliths acquired in reflection mode are shown in Figure 9g,h. The high reflectivity is consistent with the formation of a metallic film, and the etch marks conform to the container in which the monolith was molded. Thus, the resulting monoliths retain the microscale and macroscale features of the template. Furthermore, much of the PVP remains intact during the thermal processing at 200–300 °C. Thus, the monoliths represent a direct route to intermetallic/polymer composite films, which could be interesting materials for structural and corrosion-resistant applications. Burning off most of the polymer at higher temperatures yields free-standing intermetallic monoliths with minimal carbon residue.

By scaling up the reaction even further, *gram-scale bulk powders of intermetallic AuCu can be synthesized by heating*
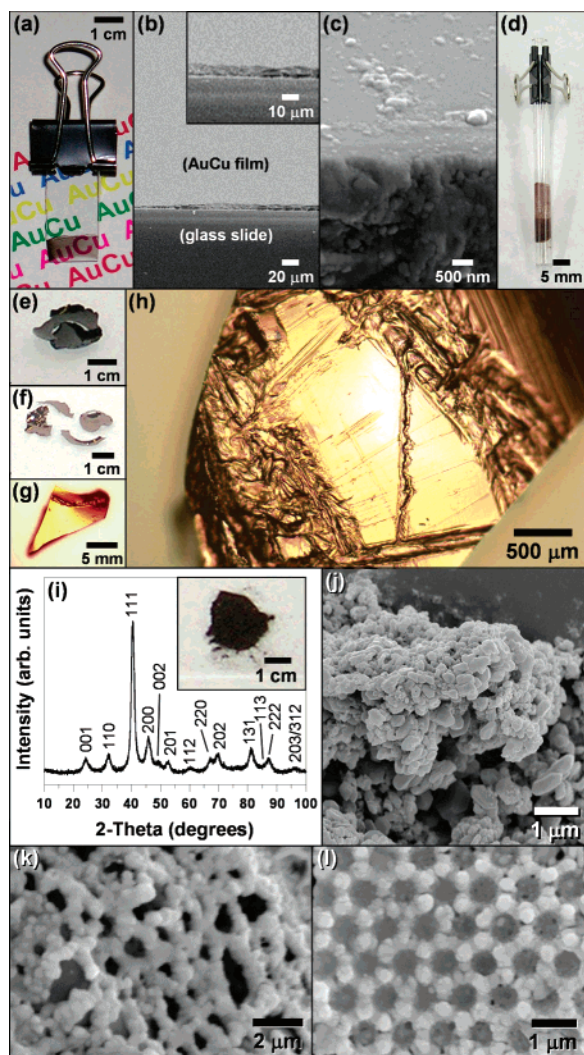
Figure 9. Morphologically diverse intermetallic AuCu nanomaterials: (a) photograph of an optically transparent intermetallic AuCu film formed by solvent evaporation and annealing at 300 °C; (b) cross-section SEM micrograph of an intermetallic AuCu film on a glass slide (showing an enlarged view in the inset); (c) high-magnification SEM micrograph of an edge of the film in (b), showing the nanoscale grains that comprise the film; (d) photograph of a 6 mm diameter glass rod coated with a film of intermetallic AuCu (the film appears darker at the bottom because it is thicker and was deposited from a solution with a higher concentration of nanocomposite precursor); (e) free-standing Au−Cu nanocomposite film prior to annealing; (f) free-standing intermetallic AuCu film after annealing at 300 °C for 30 min; (g) reflection-mode optical microscope image of a flat intermetallic AuCu free-standing film; (h) reflection-mode optical microscope image of a curved microetched intermetallic AuCu free-standing film; (i) photograph of intermetallic AuCu bulk powder (500 mg) synthesized by heating a large sample of nanocomposite powder to 300 °C for 60 min, and its corresponding powder XRD pattern; (j) SEM micrograph of sintered dense submicrometer powder of intermetallic AuCu; (k) intermetallic AuCu nanomesh; (l) intermetallic AuCu colloidal crystal replica formed by templating against polystyrene spheres.

at 300 °C for less than 1 h, since the nanocomposite precursors guarantee nanometer diffusion distances regardless of sample size. A photograph of a 0.5 g sample is shown in Figure 9i, along with its bulk powder XRD pattern, which clearly shows the formation of nanocrystalline intermetallic AuCu. Longer annealing times sinter the nanoparticles, forming dense powders with submicrometer crystallites. Figure 9j shows an SEM micrograph of the nanocrystalline intermetallic powder.
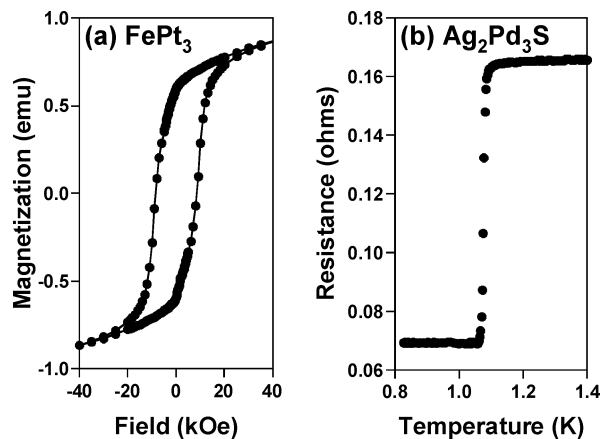

Figure 10. (a) Hysteresis loop at 10 K for an $FePt_3$ sample synthesized by heating an Fe−Pt nanocomposite to 600 °C for 60 min and (b) resistivity vs temperature from 0.83 to 1.40 K for a dense sample of superconducting Ag_2Pd_3S synthesized by heating a Ag_2S−Pd nanocomposite to 500 °C for 60 min.

Solution-templating methods for making nanostructured materials are well-known,[38−40] but related methods that form multimetallic alloy and intermetallic materials are rare.[41,42] Since the nanocomposite precursors are stable in solution, they can be infiltrated into nanoscale templates, dried, and thermally converted into alloys and intermetallics while retaining the morphology of the template. For example, a porous nanomesh of intermetallic AuCu was prepared by templating against a disordered array of polymer spheres (Figure 9k). Likewise, a periodic inverse opal structure of intermetallic AuCu was formed by templating against a colloidal crystal of polystyrene spheres (Figure 9l). Such materials are of interest for applications that include photonics, separations, sensors, and catalysts.[43]

Physical Properties. A synthetic strategy is viable if it produces new materials that have useful physical properties. Indeed, multimetallic solid-state materials made using the metallurgy in a beaker approach are functional, yielding a variety of important properties. Films of intermetallic AuCu showed a resistivity of approximately 3200 $\mu\Omega$ cm, which is 1−2 orders of magnitude higher than previously reported for bulk AuCu and may be due to grain boundary effects.[44] Field-dependent magnetic measurements confirm that our $FePt_3$ sample is a room temperature ferromagnet, with a coercivity of 8000 Oe at 10 K (Figure 10a). This compares favorably to other Fe−Pt nanomaterials, considering that the coercivity is highly variable and depends on the annealing time and temperature and the Fe:Pt ratio.[2] Figure 10b shows a plot of resistance vs temperature for

(38) (a) Holland, B. T.; Blanford, C. F.; Stein, A. *Science* **1998**, *281*, 538−540. (b) Holland, B. T.; Blanford, C. F.; Do, T.; Stein, A. *Chem. Mater.* **1999**, *11*, 795−805. (c) Yan, H.; Blanford, C. F.; Holland, B. T.; Smyrl, W. H.; Stein, A. *Chem. Mater.* **2000**, *12*, 1134−1141. (d) Jiang, P.; Bertone, J. F.; Colvin, V. L. *Science* **2001**, *291*, 453−457.
(39) (a) Martin, C. R. *Science* **1994**, *266*, 1961−1966. (b) Lakshmi, B. B.; Patrissi, C. J.; Martin, C. R. *Chem. Mater.* **1997**, *9*, 2544−2550. (c) Mitchell, D. T.; Lee, S. B.; Trofin, L.; Li, N.; Nevanen, T. K.; Soderlund, H.; Martin, C. R. *J. Am. Chem. Soc.* **2002**, *124*, 11864-11865. (d) Lee, S. B.; Mitchell, D. T.; Trofin, L.; Nevanen, T. K.; Soderlund, H.; Martin, C. R. *Science* **2002**, *296*, 2198−2200.
(40) Kim, E.; Xia, Y.; Whitesides, G. M. *J. Am. Chem. Soc.* **1996**, *118*, 5722−5731.
(41) (a) Yan, H.; Blanford, C. F.; Smyrl, W. H.; Stein, A. *Chem. Commun.* **2000**, 1477−1478. (b) Bartlett, P. N.; Ghanem, M. A.; El Hallag, I. S.; de Groot, P.; Zhukov, A. *J. Mater. Chem.* **2003**, *13*, 2596−2602.
(42) Teng, X.; Yang, H. *J. Am. Chem. Soc.* **2003**, *125*, 14559−14563.
(43) Stein, A.; Schroden, R. C. *Curr. Opin. Solid State Mater. Sci.* **2001**, *5*, 553−564.
(44) Jacobsson, P.; Sundqvist, B. *J. Phys. Chem. Solids* **1988**, *49*, 441−450.

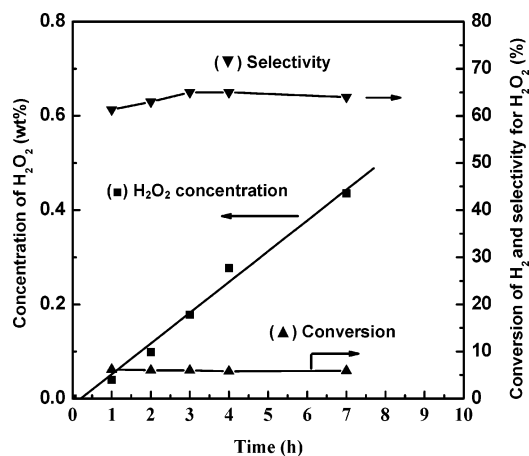**Figure 11.** Catalytic formation of H_2O_2 at 10 °C in 0.24 N H_2SO_4/ethanol (60 mL) over a PVP-stabilized $AuPd_4$ catalyst (5 mg). The O_2:H_2 ratio was 4:1, and the flow rate was 50 mL/min.

a piece of the Ag_2Pd_3S sample described in Figures 7 and 8. The data were acquired as a four-wire measurement, which included the resistance of two contacts to the sample. A sharp transition is seen near 1.10 K, where the slope reaches 8.0 Ω/K. For T < 1.10 K, the application of a magnetic field of $\mathbf{H}$ = 1.5 kOe restores the resistance to R = 0.165 Ω (not shown). These results indicate that our Ag_2Pd_3S sample is superconducting with T_c = 1.10 K. For the bulk material synthesized by a traditional solid-state reaction, T_c = 1.13 K.[37] (The resistance of the Ag_2Pd_3S sample below T_c is most likely due to contact resistance, but may also result from the large number of grain boundaries that are inherent in the low-temperature sintering process.) More detailed studies of the superconducting properties of Ag_2Pd_3S synthesized using nanoparticle precursors are currently in progress.

Despite the unknown surface chemistry of these multimetallic materials (e.g., impurities, reactivity, and accessibility of surface sites), preliminary evidence suggests that they can serve as active and selective catalysts. Figure 11 shows the catalytic formation of H_2O_2 over a $AuPd_4$ alloy catalyst. Nanocrystalline Pd is known to catalyze the formation of H_2O_2 from H_2 and O_2, and evidence exists that colloidal Pd is involved in the catalytic cycle.[45] The results in Figure 11 show that H_2O_2 is produced from H_2 and O_2 using the PVP-stabilized $AuPd_4$ alloy as a catalyst. Importantly, the selectivity for H_2O_2 formation is 65% for our unsupported $AuPd_4$ catalyst. This is significantly larger than the 45% selectivity obtained from standard Pd/SiO_2-supported catalysts.[46] These results clearly establish that (a) these multimetallic materials have accessible surfaces and (b) they can serve as stable, highly selective catalysts for important chemical transformations. Details of the surface chemistry remain unknown, and will be explored in detail in future work.

Conclusions

We have demonstrated that metal nanoparticles can be used as a robust solution-based toolkit for synthesizing intermetallic compounds and alloys within minutes at low temperatures. The strategy exploits the enhanced reactivity and nanoscale diffusion distances afforded by binary nanoparticle composites to eliminate the need for high-temperature heating and atomic-scale

homogenization, which are necessary using traditional methods for solid-state synthesis. The composition of the product is related to the composition of the metal nanoparticle precursors, and multiple compounds in the same binary system can be readily accessed; e.g., AuCu, $AuCu_3$, Au_3Cu, and AuCu-II are all accessible in the Au−Cu system. This approach is general with respect to composition, crystal structure, and morphology, and is successful for both binary and ternary phases. A significant benefit of the low-temperature solution process is that morphologically diverse nanomaterials of complex compositions and structures can be accessed—surface-confined thin films, free-standing films, nanomesh materials, inverse opals, and gram-scale bulk powders with dense submicrometer crystallites. As shown previously, this approach can also yield discrete solution-dispersible intermetallic nanocrystals in the Au−Cu system.[19] Such flexibility in materials synthesis and processing is unprecedented for intermetallics and alloys.

This approach has several important implications for synthesizing new solid-state materials and for controlling critical aspects of materials processing. The ability to synthesize multimetallic solids at low temperatures without arc-melting or high-temperature annealing shifts the rate-limiting step from solid−solid diffusion to nucleation, and thus has the potential to yield new metastable, nonequilibrium, and interfacially stabilized phases as bulk materials. Likewise, the solution-based precursors provide access to complex nanostructured materials and thin films that would otherwise be inaccessible or require high-temperature or vacuum deposition techniques. Thus, this approach could open the door to intermetallic and alloy coatings on a variety of planar and nonplanar supports, flexible films on polymer substrates, high-surface-area materials for catalytic applications, and nanotemplated materials, such as inverse opals and possibly nanorods, for fundamental studies and devices that exploit nanoscale magnetic, electronic, and optical properties.

The materials synthesized using this metallurgy in a beaker strategy are inherently impure, since the synthesis relies on sacrificial polymers and other solution additives that are necessary for reducing the metal salts and inducing nanoparticle aggregation to form nanocomposites. However, we demonstrated that these materials can have properties that are comparable to or superior to those of materials synthesized through more traditional routes that generally have higher purities. Other alternative synthetic approaches yield highly pure materials, but require much more elaborate setups and are not as amenable to scaleup (e.g., thin films prepared by Johnson and co-workers using elementally modulated reactants).[16] Our materials, although not as pure as those made by other routes, are easy to synthesize and scale up and may be appropriate for applications where low-level impurities are tolerable. There is a tradeoff between ultrapure materials and materials that are easy to process and simple to produce in large quantities with controllable compositions and morphologies. We believe that the approach described here could be a viable strategy for synthesizing complex nanostructured materials with useful, unique, and unanticipated properties.

(45) Dissanayake, D. P.; Lunsford, J. H. *J. Catal.* **2002**, *206*, 173−176.
(46) Han, Y.-F.; Lunsford, J. H. *Catal. Lett.*, in press.

Supporting Information Available: Powder XRD patterns for intermetallic AuCu synthesized from bulk precursors and using PSS and PEO, deconvoluted XPS spectrum for the Cu 2p region of the Au−Cu nanocomposite precursor, and EDS spectra for the Ag_2Pd_3S nanocomposite (PDF). This material is available free of charge via the Internet at http://pubs.acs.org.

JA043335F